Design and demonstration of tunable soft x-ray lateral shearing and Hartmann wavefront sensors

Antoine Wojdyla, Diane Bryant, Weilun Chao, Lahsen Assoufid, Daniele Cocco, et al.

Antoine Wojdyla, Diane Bryant, Weilun Chao, Lahsen Assoufid, Daniele Cocco, Mourad Idir, Kenneth A. Goldberg, "Design and demonstration of tunable soft x-ray lateral shearing and Hartmann wavefront sensors ," Proc. SPIE 10760, Advances in X-Ray/EUV Optics and Components XIII, 1076003 (17 September 2018); doi: 10.1117/12.2321642

SPIE.

Event: SPIE Optical Engineering + Applications, 2018, San Diego, California, United States

Design and demonstration of tunable soft x-ray lateral shearing and Hartmann wavefront sensors

Antoine Wojdyla*[a], Diane Bryant[a], Weilun Chao[b], Lahsen Assoufid[c], Daniele Cocco[d], Mourad Idir[e], Kenneth A. Goldberg[a]

[a]Advanced Light Source, Lawrence Berkeley National Laboratory, Berkeley, CA, USA 94710; [b]Center for X-Ray Optics, Lawrence Berkeley National Laboratory, Berkeley, CA, USA 94710; [c]Advanced Photon Source, Argonne National Laboratory, Argonne, IL, USA 60439; [d]Linac Coherent Light Source, SLAC National Accelerator Laboratory, Menlo Park, CA, USA 94566; [e]National Synchrotron Light Source-II, Brookhaven National Laboratory, Upton, NY, USA 11973-5000

ABSTRACT

We describe design guidelines for soft x-ray wavefront sensors and experimentally demonstrate their performance, comparing grating-based lateral shearing interferometry and Hartmann wavefront sensing. We created a compact shearing interferometer concept with a dense array of binary amplitude gratings in a single membrane to support one-dimensional wavefront measurements across a wide wavelength range without the need for longitudinal position adjustment. We find that a common scaling parameter based on wavelength and the distance to the measurement plane guides the design of both systems toward optimal sensitivity. We show preliminary results from recent experiments demonstrating one and two-dimensional wavefront sensing below the Maréchal criterion.

Keywords: X-ray optics, synchrotron radiation, wavefront sensing, soft x-ray, Hartmann sensors, lateral shearing interferometry, scintillator, diffraction-limited storage rings

1. INTRODUCTION

With the emergence of x-ray diffraction-limited storage rings and free-electron lasers[1] comes an increasing interest in at-wavelength wavefront sensors[2-5] to serve as diagnostics and for feedback to adjustable degrees of freedom, including adaptive optical elements. Any perturbations of the coherent photon beam generated by the ultra-low emittance electron beam can spoil the quality of the beam. Static wavefront errors arise from the additive contributions of surface and coating quality, relative alignment, and cleanliness of the optical elements within a beamline. Dynamic errors arise from vibration, drift, instability, the mis-calibration of active elements, and from uneven deformation under heat load ─which becomes an increasing concern as beam sizes get smaller and brighter[6].

Numerous methods of wavefront sensing at short wavelengths have been demonstrated in recent years. Where high coherence is available, common path interferometers─such as the *point diffraction interferometer* (PDI[7,8,9]) and the *phase-shifting point diffraction interferometer* (PS/PDI[10,11])─allow comparison with a spherical reference beam through pinhole diffraction, but they can be challenging to align and are typically applicable to small wavefront errors. Grating-based shearing interferometers rely on the self-interference of the beam; they are easy to align and operate with wider dynamic range. Such techniques include *lateral shearing interferometry* with amplitude[12] or phase gratings[4], Ronchi gratings[5] or Talbot imaging[3,13]. Non-interferometric techniques are also available where beam coherence is low or large wavefront errors must be measured. The Hartmann technique uses a static grid to measure local wavefront slope values based on the diffraction of non-interfering beamlets[2,14]. So-called *pencil beam techniques* measure wavefront slope errors using a scanning slit or pinhole. Other highly-sensitive methods that have recently been demonstrated include *speckle tracking*[15,16] and *ptychography*[17].

Among these techniques, we believe that shearing interferometry and Hartmann wavefront sensing, with their compatible measurement configurations and complementary properties, have the greatest applicability for soft x-ray applications. Once calibrated, these techniques can operate with high efficiency, high sensitivity, and they allow data collection from a single, static measurement.

Advances in X-Ray/EUV Optics and Components XIII, edited by Shunji Goto, Christian Morawe, Ali M. Khounsary, Proc. of SPIE Vol. 10760, 1076003 · © 2018 SPIE
CCC code: 0277-786X/18/$18 · doi: 10.1117/12.2321642

*awojdyla@lbl.gov; phone 1 510 486-6153

While many prior demonstrations of the Hartmann and shearing techniques have been applied to relatively wide or diverging beams[18,19,20], some new beamline wavefront feedback applications will require operation where beams are converging toward focus, and where beam diameters are less than 3 mm (Fig. 1). Furthermore, considerations of how these sensors can be used in non-invasive geometries (i.e. performing measurement on one portion of a beam after a beamsplitter), to serve as active feedback, is of high interest.

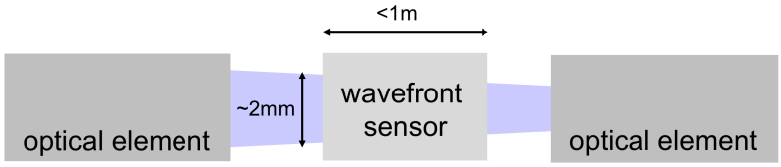

Figure 1. Monitoring wavefront sensor configuration. The wavefront sensor must intercept the beam between optical elements, while the beam has a limited footprint.

For in-situ operation on soft x-ray beamlines, a small beam footprint (typically 2 mm) and limited space between optical elements (a few meters) dictate strong design constraints. Moreover, non-invasive (or least-invasive) configurations are desirable, and keeping the imaging elements clear of the primary beam (or easily retractable) is thus necessary.

2. WAVEFRONT SENSOR DESIGN

Here we consider wavefront measurement with lateral shearing interferometry and Hartmann sensing. Both methods are applicable with comparable requirements in circumstances where power densities are low enough to permit the use of thin, membrane-based transmission elements with lithographically patterned features. The Hartmann sensor uses a binary amplitude array of (typically square) holes with relatively large separation relative to the hole size. Shearing gratings are dense, typically with equal-sized lines and spaces[21] or a checkerboard pattern[22]**.** At visible-light and hard x-ray wavelengths the use of *phase gratings* can increase the efficiency of the shearing method, but this is not necessary. At extreme ultraviolet and soft x-ray wavelengths, where absorption is high, amplitude gratings are effective. In both techniques, the light pattern is projected downstream, either onto a camera directly or onto a scintillator that is imaged onto a camera with a lens.

2.1 Shearing interferometry

For shearing interferometry, only amplitude gratings can be considered because of the strong absorption of most materials for any wavelength λ in the range of interest within the soft x-ray regime (λ = 0.9–5 nm, corresponding to a photon energy range of E_{ph} = 250–1400 eV).

Shearing interferometry relies on the Talbot self-imaging effect, in which a periodic structure forms recurring *self-images* at periodic distances. Local wavefront slope errors cause shifts in the observed positions of the grating pattern downstream that can be measured and analyzed to reconstruct the wavefront. A simple way to understand the operating principle is by recognizing that the grating acts as a beamsplitter, producing multiple, overlapping copies of the incident beam, with a small angular displacement between the beams. For a given wavelength, λ, the shear angle θ for grating period, p, satisfies the grating equation:

$$\sin\theta = \lambda/p. \quad (1)$$

At a position downstream of the grating, z, the lateral shear $\Delta s = z \sin\theta \approx z\lambda/p$, for small angles. For optimal contrast, the sensor should be placed at a distance, z_T (called the Talbot distance) where the self-imaging occurs. For the simple case of a plane-parallel incident beam, Talbot distances occur at intervals given by

$$z_T = np^2/\lambda, \quad (2)$$

where n is an integer. For detector distance z_c = 400 mm and center wavelength of λ = 2.5 nm (E_{ph} = 500 eV), this results in a grating period of p = 31.5 μm (Fig. 1.)

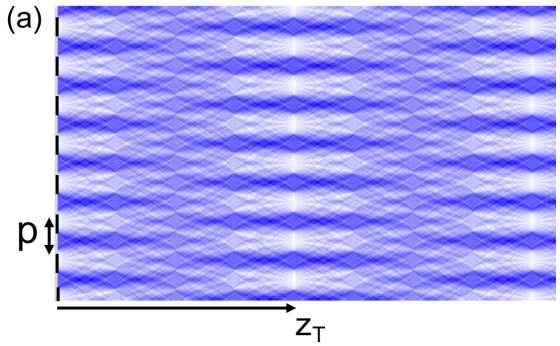

Figure 2. Diffraction from a shearing grating. Numerical simulations with a grating pitch of p = 31.5 μm for a photon energy of E = 500eV (λ = 2.5 nm) over 800 mm in a collimated beam configuration. The first Talbot distance $z_D = p^2/\lambda$ is such that orders -1,0, and 1 interfere constructively and where the fringe contrast is maximum.

We define a *shear ratio* as the shear distance Δ*s* relative to the width of the beam *s* at the measurement plane. This important factor determines the sensitivity of the technique, and it is constrained by Eq. (2). It is possible however to operate on fractional Talbot distance[4]. A small shear angle is advantageous because it enables a high degree of overlap among the adjacent beams. If the shear ratio exceeds 10% of the beam width, *s*, for example, then portions of the edges of the beam will not be measurable in a straightforward way.

The number of illuminated fringes $N_s = s/p$ also constrains the dynamic range of the technique and can be adjusted changing both the grating pitch and the camera distance accordingly to match the Talbot condition (Eq. (2).)

2.2 Hartmann sensing

For the Hartmann sensor, the local wavefront slope error is measured by finding the centroid positions of the individual diffracted beamlets, and comparing them to the positions expected from an ideal beam. To reduce possible systematic errors from intensity gradients in the incoming beam, the hole aperture a_h should be small enough so that the diffraction from these holes is fully developed (Fresnel regime.) This condition dictates that the spot size due to diffraction should approximately equal the hole size; given that the divergence half-angle of a beamlet from a hole is $\sin\theta = \lambda/a_h$, the beamlet size at distance z is approximately θz. and must satisfy $\theta z = \lambda z/a_h > a_h$, hence we find the camera must be located further than the diffraction distance z_D:

$$z > z_D = a_h^2/\lambda. \quad (4)$$

To facilitate centroid measurement, the grid spacing d has to be large enough to prevent the diffracting beamlets from overlapping at the detector plane; but it must small enough to provide sufficient sampling of the beam across its width. A *guard factor* of 8 (d_h/a_h) is enough so that the side lobes of the diffraction pattern do not overlap (Fig. 2).

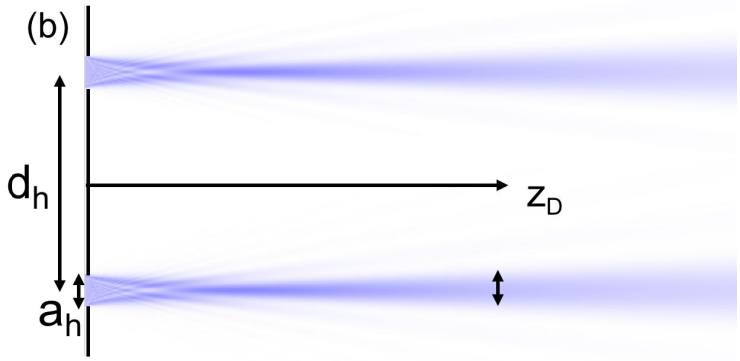

Figure 3. Diffraction from the holes of a Hartmann grid. Numerical simulations with a hole aperture a_h=18 μm and hole distance d_h = 120 μm for a photon energy of E = 500eV (λ = 2.5 nm) over 200 mm. The Fresnel distance $z_D = a_h^2/\lambda$ is such that the diffraction spot size is comparable to the hole size.

The spatial resolution of the wavefront reconstruction for the Hartmann sensor is in general lower than for shearing interferometer, with a number of samples $N = s/d_h$ where s is the size of the beam on the Hartmann grid.

2.3 Effects of convergent and divergent beams

For a shearing interferometer on a beamline, we anticipate that measured beams could be converging or diverging, depending on where they are intercepted. This property has an effect on the self-focusing distance as follows: while the convergence can be construed as an aberration (quadratic phase, corresponding to defocus), it has the effect of shifting the effective Talbot plane z_C (Fig. 4.)

Considering that the nominal Talbot distance z_T is defined as a function of the grating pitch p_0 and the wavelength λ according to $z_T = p_0^2/\lambda$, the effective Talbot distance z_C is the location where the apparent pitch $p = (z_F - z)/z$ (i.e. the magnification of the pitch at a distance z) is equal to the pattern shift $\Delta = \lambda/d_0 \cdot z$ at the same distance. We thus have:

$$\begin{aligned} \lambda/p_0 \cdot z_C &= p_0 \cdot (z_F - z_C)/z_F \\ \lambda/p_0^2 &= (z_F - z_C)/z_F z_C \\ 1/z_T &= 1/z_C - 1/z_F \\ 1/z_C &= 1/z_T + 1/z_F \end{aligned} \quad (5)$$

When the beam is collimated, the effective Talbot distance is equal to the nominal Talbot distance, namely the distance at which the shear is equal to one grating period; this is the plane where the fringe contrast is maximum.

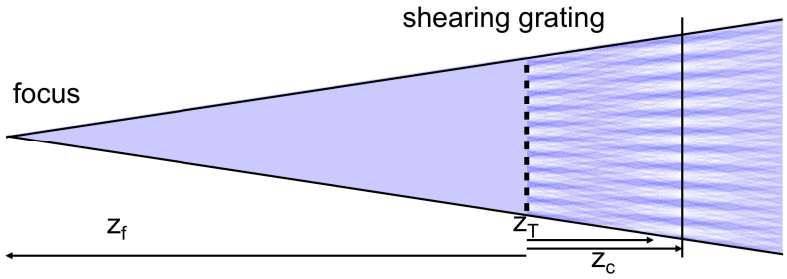

Figure 4. Effective Talbot distance in shearing interferometry for a divergent beam. Numerical simulations for a grating pitch p = 31.5 μm, a distance to focus z_F = -2.4m and a wavelength λ = 2.5 nm. The nominal Talbot distance is z_T = 400mm and the effective Talbot distance is z_c = 480mm.

While the beam divergence is often leveraged to allow geometrical magnification and the use of finer features on the shearing grating or the Hartmann grid ($z_F << z_C$), potentially improving sensitivity, spatial resolution and dynamic range, divergence effects should be considered as perturbations to the collimated case for in-situ wavefront sensing.

2.4 Optimal dimensions for in-situ wavefront sensing and indirect detection using a scintillator

The similarity between Eqs. (1) and (3), with the sensor distance z dependent on the square of the critical dimension a (shearing grating period or Hartmann grid hole size), makes the Eq. 4 a general design principle for shearing and Hartmann wavefront sensors. For a fixed distance z_c between the grating and the detection plane, this equation sets the optimal grating pitch for a given wavelength:

$$a = \sqrt{z_c \lambda}, \quad (5)$$

For most reasonable sensor distances (e.g. 0.1 to 1 m) and wavelength range (from 500 eV to 20 keV), the feature size lies between 5 and 50 μm. While a smaller feature size can be used in cases where the grating or the grid is located close to focus and gets magnified, this is usually not the case for in-situ wavefront sensor configurations, and the optical resolution of the camera itself needs to be below 5 μm to capture the fringes and diffraction spots.

Direct detection with a short-wavelength CCD camera is problematic owing to the relatively large pixel sizes of available in-vacuum cameras. Pixels in the 10 μm range are incompatible with the measurement length scales defined above and cannot provide sufficient resolution. Having smaller pixels would decrease the dynamic range of the camera, meaning it would saturate quickly.

Therefore, we opted for using a scintillator (typically a YAG:Ce), which converts high energy photons into visible photons, then reimaged onto a camera with some magnification. The reimaging in the visible range has the additional advantage that it allows the use of a fold mirror (in our case, a prism) in the optical system, so that the camera itself can stay clear of the beam. However, the inclusion of additional elements imparts perturbations to the detected wavefront, in the form of systematic errors, requiring calibration to achieve a certain level of accuracy for absolute measurements. The wavefront sensing can easily be adapted from 1D to 2D configurations with the same dimensions. For real-time wavefront monitoring applications in future ALS beamlines, we are primarily interested in 1D designs since they are directly applicable to 1D adaptive mirror shape feedback. In addition, they are more light-efficient.

3. WAVEFRONT SENSOR PROTOTYPE

The simple and versatile soft x-ray wavefront sensor developed here is designed for operation in ultra-high vacuum (UHV), primarily over the photon energy range, 250–1400 eV, which can be extended (a schematic and photo are shown in Fig. 6)**.** The central concept is to position the shearing gratings and the Hartmann grids in separate longitudinal planes, where they can be rapidly inserted or withdrawn from the beam on linear translation stages. The stages allow the beam to pass through one of several different transmission gratings or grid membranes that have been lithographically fabricated on silicon wafer chips. This allows us to switch among measurement methods in seconds, and to select gratings and grids that are most appropriate for the beam energy.

Downstream of the transmission elements the beam reaches a stationary YAG:Ce scintillator glued to one 5-mm face of a 45° glass prism that reflects the image upward through an optical flat (which also serves as a vacuum window), and into the imaging system (Fig. 6a.) The microscope objective is a 5×/0.12NA long working distance (34 mm) microscope objective (Mitutoyo MY5X-802), a tube lens (Mitutoyo MT-1) focusing on a visible light camera. The camera (Basler acA4112–20um with Sony IMX304 CMOS sensor) has 3000 × 4096 pixels with 3.45 μm pixel size, thus providing an effective field of view of 2.0 mm × 2.8 mm.

In our prototype system, the shearing gratings are 400 mm upstream of the YAG; the Hartmann grids are 100 mm upstream. The short soft x-ray attenuation lengths in the YAG material (μ_{YAG} = 0.1–2.0 μm) means that the image is formed close to the front surface of the YAG. Furthermore, the YAG thickness of 50 μm was selected to approximately match the depth of focus of the microscope lens[23]. For this reason, the telecentricity of the microscope lens is not a significant concern, as it could be with higher energy, more penetrating beams.

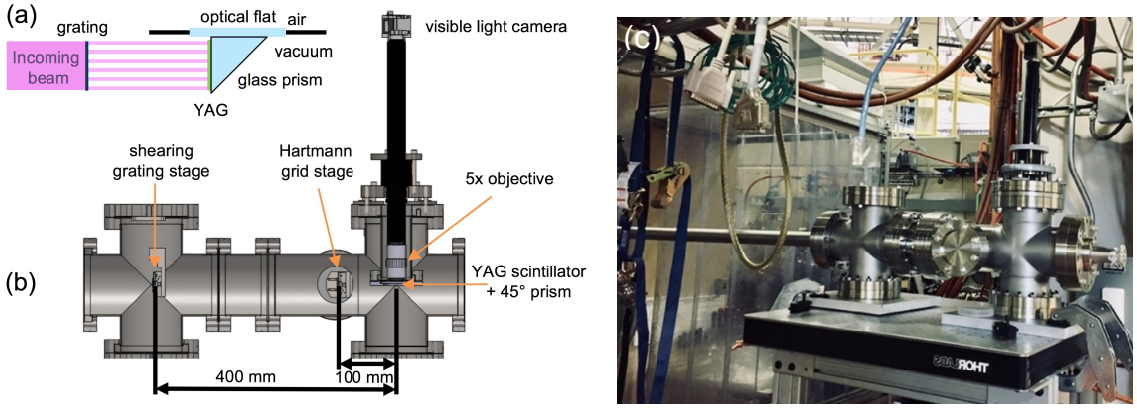

Figure 6. Soft x-ray wavefront sensor. (a) Schematic of the wavefront sensor with the in-vacuum indirect detection scheme (b) Schematic of the wavefront sensor inside a vacuum vessel, with two linear stages to support shearing and Hartmann gratings, a YAG:Ce scintillator glued on a prism and an optical flat at the vacuum-air interface, and the imaging system at air. (c) The wavefront sensor installed on beamline 6.3.2 at the Advanced Light Source.

While some authors have begun using YAG:Ce-coated in-vacuum visible-light cameras[2] (with lesser resolution but greater light efficiency), we opted for simplicity, using readily available components without significant vacuum compatibility concerns or in-vacuum thermal management requirements.

The binary amplitude gratings were fabricated in 100-nm-thick gold patterns on 2-mm square 100-nm-tick silicon-nitride windows. They were manufactured using contact photolithography and electroplating. The gratings were assembled in groups of four on silicon wafer chips, plus an empty window, as shown in Fig. 5.

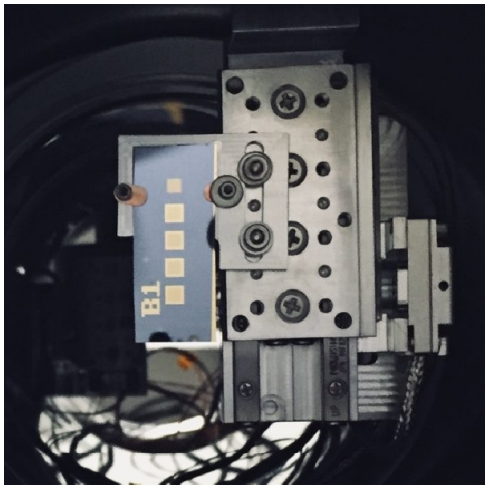

Figure 5. Grating chips. (left) Grating chip layout, with 18.8, 22.3 μm, 31.5 μm and 44.5 μm pitch shearing gratings, to cover the 250–1400 eV range, and one empty window. (right) Grating chip mounted on a linear stage inside a vacuum vessel, to allow easy switching between grating pitches.

Before final assembly, we calibrated the reimaging optics magnification by recording images of a 200 line/mm Ronchi ruling. We found the magnification to be within 0.1% of the design. The observed distortion at the edge of an image was measured to be 612 ± 57 nm peak-to-valley (PV). Therefore, for a 30-μm-pitch shearing pattern, uncalibrated distortion would appear as a $\lambda/50$ PV systematic error. This magnitude is consistent with the accuracy reported by Liu on a comparable system before calibration[4].

The effective magnification of the system is 5.00x. The addition of glass in the optical path does change the effective focal length, but the magnification remains the same. We predicted the vacuum/atmospheric differential pressure on the optical flat to induce a 1.6 μm deflection at the center of the 2-inch diameter, 3-mm-thick optical flat. Combined with the spherical aberration caused by the presence of glass, the imaging performance remains diffraction limited, with 200 lines/mm grating clearly resolved ($0.61\lambda_{YAG}$/NA=2.8μm).

The optical elements were pre-aligned on an optical bench using a 5 mW He-Ne laser, before installation on ALS bending-magnet beamline 6.3.2 (Fig. 6c.) Residual misalignment of the stage axes caused the gratings windows to reduce useful field of view to 1.8 mm x 1.5 mm in our first round of experiments.

4. RESULTS

First experiments were performed on beamline 6.3.2 of Lawrence Berkeley National Laboratory's Advanced Light Source. While this bend magnet beamline[24] has a photon energy range of 50–1300 eV, we performed the majority of our experiments at 500 eV, with flux of about $8x10^{10}$ ph/sec and a 1:1500 spectral bandwidth. The beam size at focus was 50um x 100um, with divergence 1mrad x 0.5mrad. The shearing grating was located 2.5 m from focus, so that the beam would be overfilling the sensor. At this flux level, we set the acquisition time of the camera to 10 seconds, recording multiple repeats for data accumulation where necessary.

We recorded data using a variety of horizontal and vertical 1D shearing gratings. Horizontal fringes are shown in Fig. 7a. The 10 μm vertical source size in today's ALS imparts significantly higher coherence in the vertical direction than in the horizontal, where the beam size is 250 μm. This contributes to higher fringe contrast in the vertical direction (horizontal fringes). For 1D data collection, the image data can be integrated in the direction parallel to the fringes to significantly improve the signal to noise ratio, relative to 2D wavefront measurements.

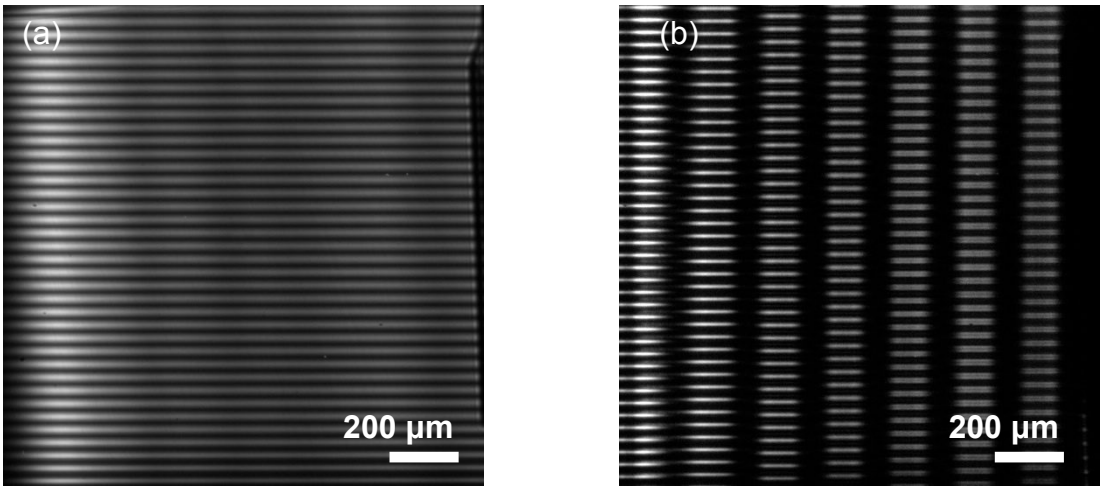

Figure 7. Shearing interferometry. (a) Horizonal 1D shearing grating with 31.5 µm pitch. The spatially varying intensity arises from non-uniformities in the beam. (b) Multi-wavelength shearing gratings with pitch [30.2-33.3 µm].

We also collected data to demonstrate the 1D multi-grating principle (Fig 7b). Here, the gratings form an array with a different pitch in each grating. For wavelengths within the operating range, there will always be at least one grating projecting high-contrast fringes close to the Talbot condition.

Both 1D and 2D Hartmann wavefront sensor data was collected using the grids on the downstream stage (Fig. 8a and 8b)

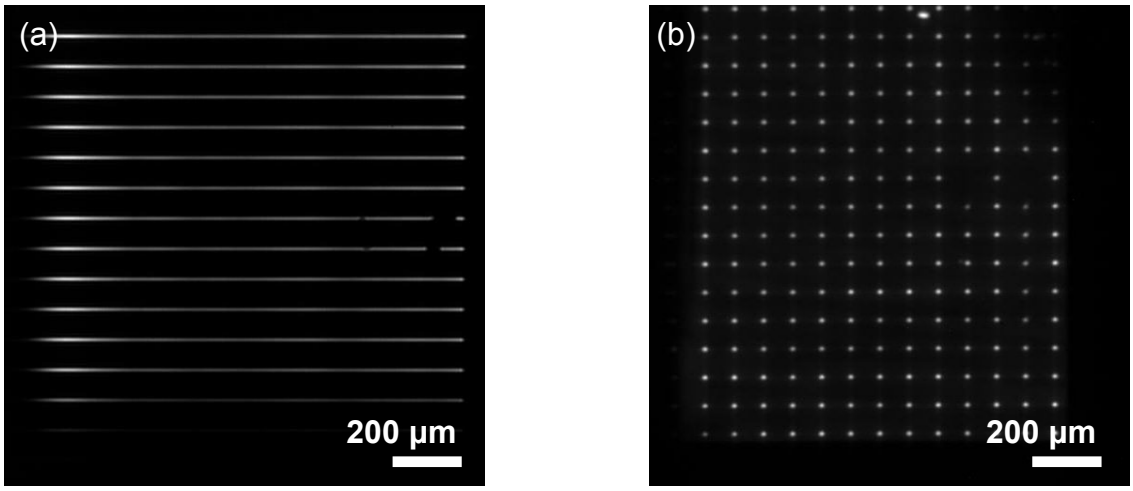

Figure 8. **Hartman grids**. (a) 1D Hartmann grid with 18 µm width and 120 µm spacing. (b) 2D Hartmann grid, with the same parameters.

To assess the stability of the system, we used the zero order beam with a glass filter in order to perform fast data acquisition (5 msec exposure time). We were able to measure that the vibration of the camera was below 1.5 µm. For longer exposure time, the repeatability of the centroiding procedure for a single spot along the vertical direction was below ε_{spot} = 0.074 px-rms, corresponding to $\varepsilon_H = \varepsilon_{spot} \cdot D/L$ =51 pm ~ λ/50-rms at 500 eV.

5. WAVEFRONT RECONSTRUCTION

The wavefront measurements described above enable beam characterization and the comparison of the two measurement methods, under various conditions. Careful calibration for accuracy requires a reference wave or an independent measurement, and it has not yet been included**.** Estimations of the systematic error is in the range of $\lambda/50$ (PV) and should not affect the accuracy.

We performed a reconstruction of the wavefront at a 2.5-nm wavelength (E_{ph} = 500 eV) using both shearing interferometry and Hartmann sensing.

For shearing interferometry, a grating with pitch 31.5 μm was selected (z_c = 400 mm), with the scintillator 400 mm downstream of the grating. The total exposure time was 10 seconds, and we collected 32 independent measurements to assess the stability of the wavefront error reconstruction (Fig. 9a.)

For the reconstruction of the wavefront[25], the recorded image $i(x,y)$ is summed along the horizontal direction (1500 pixels) to give the shearing pattern $I(y) = \Sigma_x I(x,y)$. The shearing pattern is then filtered and demodulated in the Fourier domain around the spatial frequency corresponding to the grating pattern, to yield the wavefront slope $S(y)$. The integration of the slope error along the pupil results in the wavefront $W(y)$.

After removal of the quadratic term in the wavefront shape, we measured a residual wavefront error of $\lambda/4$-rms (Fig. 9b), The aberration is dominated by a 3rd order, coma shape.

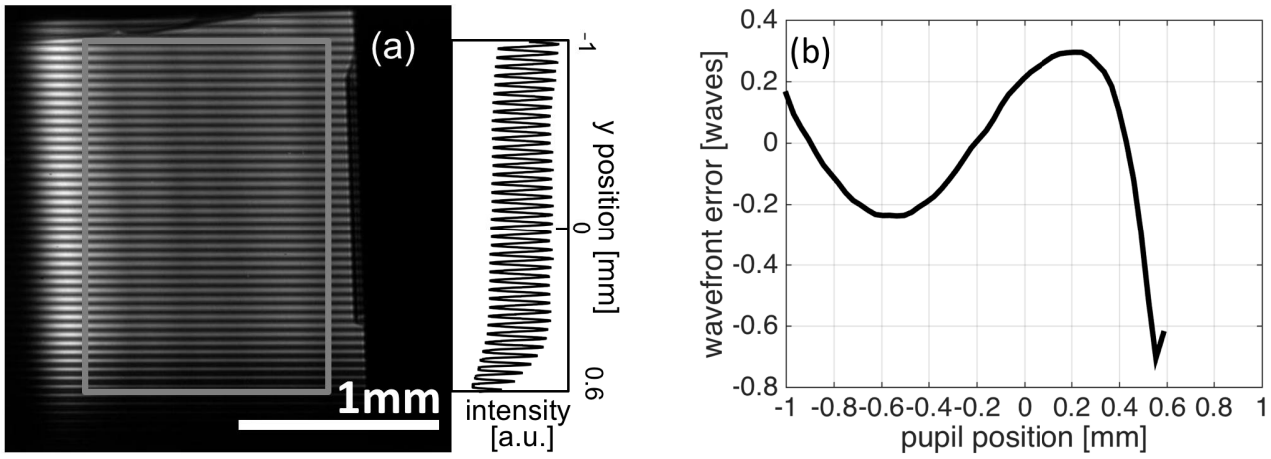

Figure 9. Reconstruction of the aberrations from shearing interferometry measurements at 500eV. (a) Image of the shearing pattern acquired on the camera (the box denotes the region used for the reconstruction). (d) Reconstructed wavefront error, with tilt and defocus term removed.

By comparing the results of 32 independent measurement acquired successively, it is possible to estimate the effect of shot noise and vibrations on the precision. The repeatability of the reconstruction is $\lambda/1500$-rms.

The Hartmann data was recorded on a grid with a_h=18 μm slits and d_h=120 μm period, with the scintillator z_c=100 mm downstream of the grid (Fig. 10a.) The acquisition was 10 sec.

The reconstruction procedure starts with an averaging along the line, to increase the signal-to-noise (Fig. 10b), then the centroids $y_c = \Sigma y I(y)/\Sigma I(y)$ are computed for each line, on the domain for which the line intensity I is above a certain threshold depending on the noise level. The relative distance between each centroid` yields the slope $S(y) = y_c(y)/z_c$, to which we subtract the linear trend (corresponding to defocus; the linear trend can be kept in the case of a well-calibrated system.) The wavefront error is the slope error integrated over the pupil.

The reconstruction without calibration shows a residual wavefront error of 0.623 nm rms (~$\lambda/4$ rms, Fig.10c.)

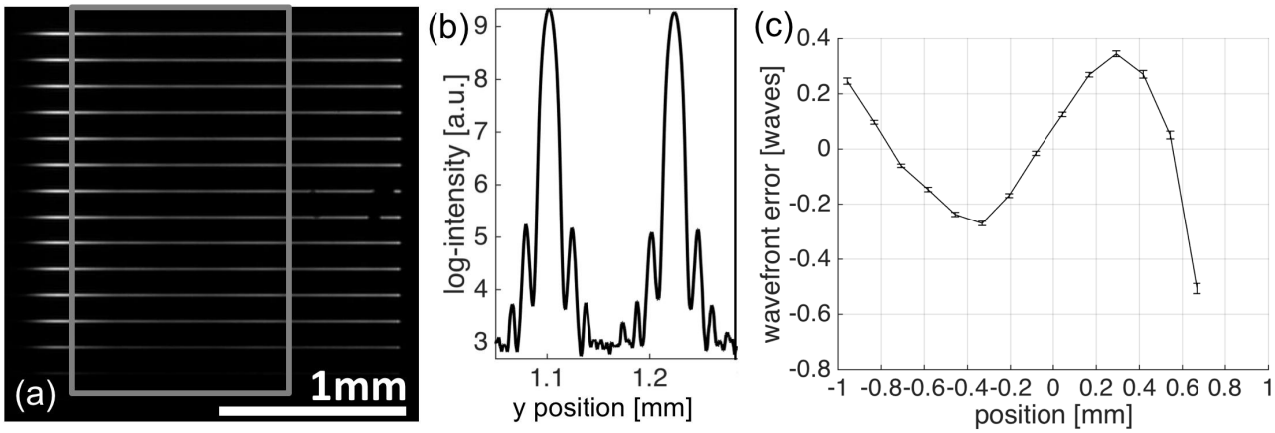

Figure 10. Reconstruction of the aberrations from the Hartmann sensor measurement at 500 eV. (a) Image of a Hartmann pattern acquired on the camera (shown is for 32x10sec exposure time.) (b) Two Hartmann lines averaged along the horizontal dimension. (c) Reconstructed wavefront error (with tilt and defocus removed.)

Repeats of the data collected at wavelength for 10 second exposure time suggest a precision for the Hartmann sensor of about λ/100-rms (Fig. 10c), owing to the fact that the Hartmann sensor is less light-efficient than the shearing interferometer and might also be more susceptible to vibration and drift.

Direct comparison of the independently measured and reconstructed 1D wavefronts profiles, based on subtraction of the two wavefronts, shows a residual difference magnitude of λ/35 rms, and λ/55 rms difference in the projection on orthonormal polynomial basis (Fig. 11.) While there is more work to be done in characterizing accuracy, this level of agreement exceeds our initial expectations. The techniques and reconstruction methods are different, and the sampling density is lower with the Hartmann sensor.

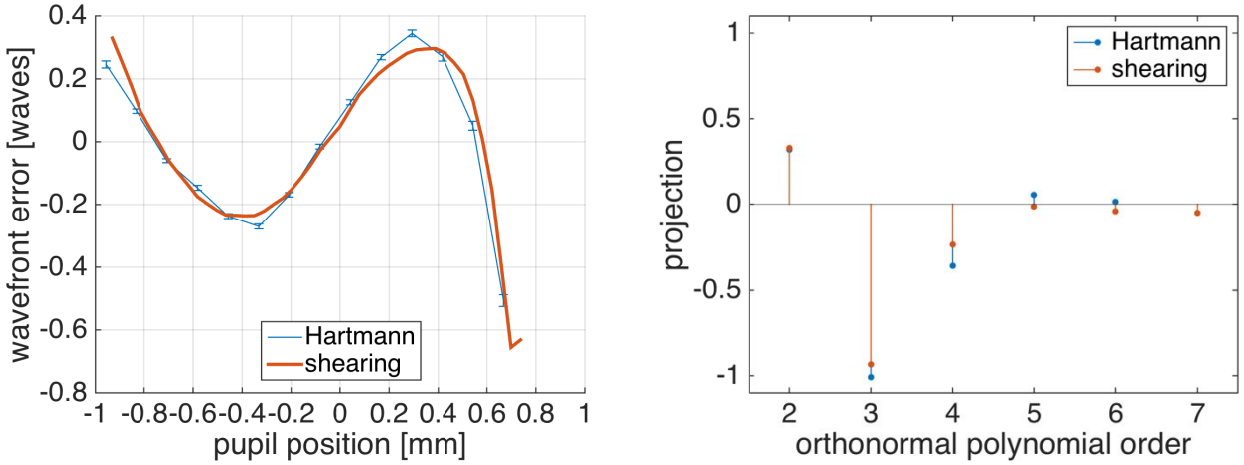

Figure 11. Comparison between the wavefront reconstruction from the shearing interferometer and the Hartmann sensors. (left) Variation of the aberration at LH (with defocus term removed); the difference between the two measurements is λ/78 rms. (right) Projection of the wavefront errors on an orthonormal polynomial basis.

6. CONCLUSION

We have developed a design methodology for short wavelength x-ray shearing and Hartmann wavefront measurement systems, and applied it to a versatile prototype sensor test platform. In particular, our approach addresses the design constraints of small, converging beams, which are expected from future, high-brightness beamlines on an upgraded

Advanced Light Source. Our soft x-ray wavefront sensor was designed to operate in vacuum, with photon beam energies in the 250–1400 eV energy range, although the principle is applicable to a wide range of EUV and tender x-ray energies as well. With independent measurement and reconstruction, the observed wavefront errors from shearing interferometry and Hartmann sensing were 0.623 nm and 0.624 nm, respectively, across a beam width of 1.5 mm. Even without calibration, direct comparison of the wavefronts showed a residual difference of 0.071 nm rms. We will proceed to further experiments so as to calibrate the sensor to determine its accuracy. We also want to investigate the effect of finite bandwidth (for non-monochromatized beams) and refine the analysis for cases where the measurements are not in the Talbot plane.

ACKNOWLEDGEMENTS

The authors would like to thank CXRO scientists Sharon Oh, and James McDougal for the manufacturing of the gratings, Ryan Miyakawa for his help with the design of the gratings, and Erik Gullikson for his help with the operation of beamline 6.3.2 at ALS.

This work is supported under DOE contract DE-FOA-0001414, from the office of Basic Energy Sciences, and was performed by the University of California, Lawrence Berkeley National Laboratory under the auspices of the U.S. Department of Energy, Contract No. DE-AC02-05CH11231.

REFERENCES

[1] Yabashi, M., & Tanaka, H., "The next ten years of X-ray science," Nature Photonics, 11(1), 12 (2017).
[2] Keitel, B., Plonjes, E., Kreis, S., Kuhlmann, M., Tiedtke, K., Mey, T., Schäfer, B. and Mann, K., "Hartmann wavefront sensors and their application at FLASH," Journal of Synchrotron Radiation, 23 (43) (2016).
[3] Grizolli, W. C., Shi, X., Assoufid, L., Kolodziej, T. and Shvyd'ko, Y., "Single-grating Talbot imaging for wavefront sensing and x-ray metrology," Proc. SPIE 10385 (2017).
[4] Liu, Y., Seaberg, M., Zhu, D., Krzywinski, J., Seiboth, F., Hardin, C., Cocco, D., Aquila, A., Nagler, B., Lee, H., Boutet, S., Feng, Y., Ding, Y., Marcus, G. and Sakdinawat, A., "High-accuracy wavefront sensing for x-ray free electron lasers," Optica, 5(8), 967 (2018).
[5] Nagler, B., Aquila, A., Boutet, S., Galtier, E. C., Hashim, A., Hunter, Galtier, E., Hashim, A., Hunter, M., Liang, M., Sakdinawat, A., Schroer, C., Schropp, A., Seaberg, M., Seiboth, F., Van Driel, T., Xing, Z., Liu, Y. and Lee, H., "Focal Spot and Wavefront Sensing of an X-Ray Free Electron laser using Ronchi shearing interferometry," Scientific Reports, 7 (1) (2017).
[6] Zhang, L., Sánchez Del Río, M., Monaco, G., Detlefs, C., Roth, T., Chumakov, A. I. and Glatzel, P., "Thermal deformation of cryogenically cooled silicon crystals under intense X-ray beams: Measurement and finite-element predictions of the surface shape,". Journal of Synchrotron Radiation, 20(4), 567 (2013).
[7] Linnik, W. P., "A simple interferometer for the investigation of optical systems," Proceedings of the Academy of Sciences of the USSR, 1, 208 (1933).
[8] Smartt, R. N. and W. H. Steel, "Theory and application of point-diffraction interferometers (telescope testing)," Japan. J. of Appl. Phys. 14 (Suppl. 14-1), 351 (1975).
[9] Goldberg, K. A., R. Beguiristain, and J. Bokor, et al., "Progress towards λ/20 extreme ultraviolet interferometry," Journal of Vacuum Science & Technology B, 13 (6), 2923–27 (1995).
[10] Medecki, H., E. Tejnil, K. A. Goldberg, J. Bokor, "Phase-shifting point diffraction interferometer," Optics Letters, 21 (19), 1526–28 (1996).
[11] Goldberg, K. A., E. Tejnil, S. H. Lee, et al., "Characterization of an EUV Schwarzchild objective using phase-shifting point diffraction interferometry," Proc. SPIE, 3048, 264–70 (1997).
[12] Naulleau, P. P., Goldberg, K. A. and Bokor, J., "Extreme ultraviolet carrier-frequency shearing interferometry of a lithographic four-mirror optical system," Journal of Vacuum Science 18 (6), 2939 (2000).
[13] Momose, A., Kawamoto, S. and Koyama I., "X-Ray Talbot Interferometry for Medical Phase Imaging," AIP Conference Proceedings, 716 (2004).

[14] Mercère, P., Zeitoun, P., Idir, M., Le Pape, S., Douillet, D., Levecq, X., Dovillaire, G., Bucourt, S., Goldberg, K., Naulleau, P. and Rekawa, S., "Hartmann wavefront measurement at 134 nm with $\lambda_{EUV}/120$ accuracy," Optics Letters, 28(17), 1534 (2003).
[15] Bérujon, S., Ziegler, E., Cerbino, R. and Peverini, L., "Two-dimensional x-ray beam phase sensing," Physical Review Letters, 108(15), 1 (2012).
[16] Wang, H., Kashyap, Y. and Sawhney, K., "Speckle based X-ray wavefront sensing with nanoradian angular sensitivity," Optics Express, 23(18), 23310 (2015).
[17] Schropp, A., Hoppe, R., Meier, V., Patommel, J., Seiboth, F., Lee, H. J., Nagler, B., Galtier, E., Arnold, B., Zastrau, U., Hastings, J., Nilsson, D., Uhlén, F., Vogt, U., Hertz, H. and Schroer, C. G., "Full spatial characterization of a nanofocused x-ray free-electron laser beam by ptychographic imaging.," Scientific Reports, 3, 1633 (2013).
[18] Mercère, P., Idir, M., Moreno, T., Cauchon, G., Dovillaire, G., Levecq, X., … Zeitoun, P., "Automatic alignment of a Kirkpatrick-Baez active optic by use of a soft-x-ray Hartmann wavefront sensor," Optics Letters, 31(2), 199 (2006).
[19] Idir, M., Mercere, P., Modi, M. H., Dovillaire, G., Levecq, X., Bucourt, S., Escolano L. and Sauvageot, P. "X-ray active mirror coupled with a Hartmann wavefront sensor," Nuclear Instruments and Methods in Physics Research, Section A: Accelerators, Spectrometers, Detectors and Associated Equipment, 616(2–3), 162 (2010).
[20] Ribič, P. R., Rösner, B., Gauthier, D., Allaria, E., Döring, F., Foglia, L., Giannessi, L., Mahne, N., Manfredda, M., Masciovecchio, C., Mincigrucci, R., Mirian, N., Principi, E., Roussel, E., Simoncig, A., Spampinati, S., David, C. and De Ninno, G., "Extreme-ultraviolet vortices from a free-electron laser," Physical Review X, 7(3), 1 (2017).
[21] Zanette, I., David, C., Rutishauser, S. and Weitkamp, T. 2D grating simulation for X-ray phase-contrast and dark-field imaging with a Talbot interferometer. AIP Conference Proceedings, 1221, 73 (2010).
[22] Marathe, S., Shi, X., Khounsary, A. M., Wojcik, M. J., Kujala, N. G., Macrander, A. and Assoufid, L., "Development of single grating x-ray Talbot interferometer as a feedback loop sensor element of an adaptive x-ray mirror system. Proc. SPIE, 9208, 92080D (2014).
[23] Xie, H., Du, G., Deng, B., Chen, R. and Xiao, T., "Study of Scintillator thickness optimization of lens-coupled X-ray imaging detectors," Journal of Instrumentation, 11(03), C03057–C03057(2016).
[24] Underwood, J. H. and Gullikson, E. M., "Beamline for measurement and characterization of multilayer optics for EUV lithography" Proc. SPIE 3331 (52) (1998).
[25] Takeda, M., Ina, H. and Kobayashi, S., "Fourier-transform method of fringe-pattern analysis for computer-based topography and interferometry," Journal of the Optical Society of America, 72(1), 156 (1982).